Acta Geotechnica (2012) 7:139–150
DOI 10.1007/s11440-012-0159-6

RESEARCH PAPER

Consequences on water retention properties of double-porosity features in a compacted silt

Francesca Casini · Jean Vaunat · Enrique Romero · Augusto Desideri

Received: 2 September 2011 / Accepted: 23 January 2012 / Published online: 25 February 2012

Abstract The paper deals with an experimental investigation aimed at studying microstructural features and their consequences on water retention properties of statically compacted unsaturated silt. The evolution of the microstructure of the aggregate fabric induced by compaction is investigated by studying the pore size distribution changes under different initial conditions (void ratio and water content). The material used is low plasticity silt from Jossigny near Paris, France. A series of mercury intrusion porosimetry tests (MIP) were performed at different void ratios and water contents to provide microstructural information. The arrangement of aggregation/particles and pore network was also investigated with environmental scanning electron microscopy (ESEM). The MIP data were used to determine the water retention curve on drying for the specific pore network configuration induced on compaction. The MIP data were used to formulate and calibrate a multimodal water retention model for a specific pore network configuration, which is obtained by linear superposition of subcurves of a modified van Genuchten type. The study is then complemented with controlled suction oedometer tests on compacted samples to obtain the water retention properties of the material at two different void ratios. Finally, we compare the water retention properties obtained by the simulated progression of the different pore network configurations induced on the hydraulic path with the water retention properties under suction-controlled conditions. Good agreement between the two methods for the drying path is reached.

Keywords Compacted soil · Pore network model · Pore size distribution · Water retention curve

1 Introduction

Compacted soil can be seen as an assemblage of particles and aggregations having sizes that mainly depend on the compaction water content [27]. To understand how these soils behave as a composite body, one must consider the manner in which the various particles and aggregates are packed together forming a pore network, which depends on void ratio and water content at compaction. Advances in laboratory testing procedures such as mercury intrusion porosimetry (MIP), useful to study the pore size distribution, and environmental scanning electron microscopy (ESEM), able to visualise microstructural features at different hydraulic states, led to better understanding of the *soil structure* evolution during hydro-mechanical loading (e.g. [7, 8, 13–15, 20, 24, 26, 29, 30]).

The structure of most coarse-grained (or granular) soils displays a dominant monomodal pore size distribution, as there is little tendency to form aggregations. As the amount

F. Casini (✉)
Institute for Geotechnical Engineering, HIL C 33.3, ETH, Swiss Federal Institute of Technology Zurich, Wolfgang Pauli Strasse 14, 8093 Zurich, Switzerland
e-mail: francesca.casini@igt.baug.ethz.ch; francesca.casini@upc.edu

J. Vaunat · E. Romero
Departamento de Ingeniería del Terreno, Cartográfica y Geofísica, c/Jordi Girona 1-3, Universitat Politècnica de Catalunya, 08034 Barcelona, Spain
e-mail: jean.vaunat@upc.edu

E. Romero
e-mail: enrique.romero-morales@upc.edu

A. Desideri
Dipartimento di Ingegneria Strutturale e Geotecnica, Sapienza Università di Roma, via Eudossiana 18, 00184 Roma, Italy
e-mail: augusto.desideri@uniroma1.it

of fines increases, particles tend to group themselves into larger aggregates, whose size depends on the amount of water added. Soils (with an appreciable content of clay) compacted dry of optimum moisture content generally exhibit a fabric made up of aggregates of varying sizes and tend to have a bimodal pore size distribution, whereas soils compacted wet of optimum tend to display a dominant peak [8, 12]. It has been widely accepted that the different behavioural features observed on soils compacted dry or wet of optimum moisture content are almost exclusively due to different structures set up during the process of compaction (e.g. [11]). When aggregates are present, it is possible to divide the pore size distribution into two distinguishable ranges, namely, macropores and micropores. The macropores are mostly the inter-aggregate pores between aggregations, whereas the micropores are the intra-aggregate pores inside these elementary units.

In the literature, few works on the microstructural behaviour on compaction are devoted to low-activity soils with clay content less than 25% (see, for example, [8]). These silty soils have a low tendency to form aggregates (especially at low water contents), which are difficult to detect, and thus, they present a microstructure usually characterised by a monomodal pore size distribution. This aspect makes them not so attractive for the study of microstructural features. Nevertheless, with increasing water content, the aggregated structure is highlighted, developing two clear dominant modes. The current paper studies a compacted silty material and specifically focuses on the development and changes undergone on the aggregated structure induced on compaction at different initial conditions. The aggregation of the silty soil investigated at lower content is a starting assumption that will be validated later on by ESEM tests.

A deeper understanding of how microstructural features affect the water storage mechanisms of a compacted soil is of particular importance in earthworks engineering. The water retention curve expressed in terms of water content or degree of saturation and suction is hysteretic, stress path dependent (void ratio) and depends on the pore network [1, 10, 16, 18, 19, 21, 23, 25, 27, 28, 31]. To properly describe its evolving water retention character, a multimodal retention model is proposed in the paper by considering a linear superposition of two subcurves of the van Genuchten [33] type. The model is constructed based on MIP data at specified initial state, and thus, it is representative of this initial pore network configuration. The different model parameters are fitted and their evolution with water content and void ratio studied. The evolving nature along generalised stress paths (with varying void ratio and water content) is taken into account by updating the pore network configuration as the hydraulic paths develop. Simulated water retention results are finally compared with controlled-suction oedometer tests, in which different wetting and drying paths are carried out at different initial void ratios. In this way, the capability of the proposed multimodal water retention model is analysed and discussed.

2 Material used in the research

The material used in the experimental programme is an aeolian silt retrieved from a layer of alluvial soil located at Jossigny, east of Paris, France. The behaviour of the saturated and unsaturated state of this material has been studied by various authors [4, 5, 6, 34]. The physical properties of Jossigny silt are reported in Table 1. The soil is classified as low-plasticity silt (CL) (Fig. 1) with a clayey fraction of 25%. Clay minerals determined by X-ray diffractometry are illite, kaolinite and inter-stratified illite–smectite. No significant swelling properties on compacted states have been observed on wetting [17].

The grain size distribution of the soil and the grain size distribution function are shown in Fig. 1. As observed, a dominant particle size is 20 μm (within the silty size domain). It is expected that this dominant particle size is assembling the shielding skeleton of the material and that aggregations are mainly connecting and covering silty grains. An inter-grain pore size of around 20% of the particle size and around 4 μm is expected to prevail in this shielding skeleton, which will be discussed in terms of the pore size distribution data presented in the next section.

Several samples of Jossigny silt were statically compacted at constant water content $w_o = (12.8 \pm 0.5)\%$ and at different void ratios. The samples were then saturated under oedometer conditions at constant vertical stress $\sigma_v = 100$ and 200 kPa by Casini [4]. The volume change results ($\Delta\varepsilon_{asat}$, collapse on soaking) are plotted in Fig. 2 in terms of the normalised variable $\Delta\varepsilon_{asat}/\sigma_{vsat}$ for the different initial void ratios studied. The compaction induces a reduction in the macroporosity (inter-grain porosity), as highlighted by Or [22] the collapse of voids is due to

Table 1 Physical properties of Jossigny silt

Unit weight of solids γ_s (kN/m^3)	Plastic limit wP (%)	Liquid limit wL (%)	Plasticity index IP (%)	Clay fraction (%)	Silt fraction (%)	Sand fraction (%)
26.4	17	32.3	15.3	25	70	5

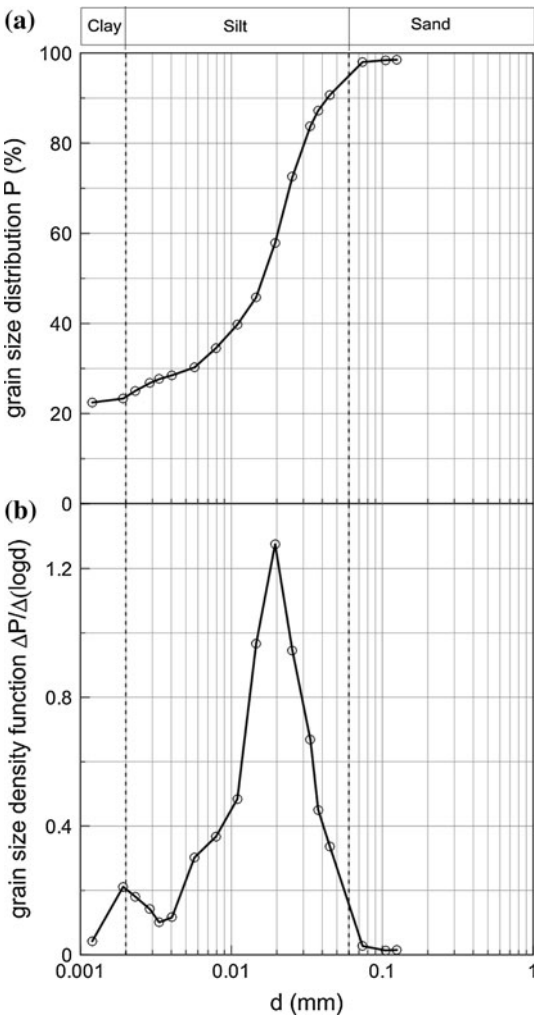

Fig. 1 Jossigny silt: **a** Grain size distribution; **b** Grain size density function

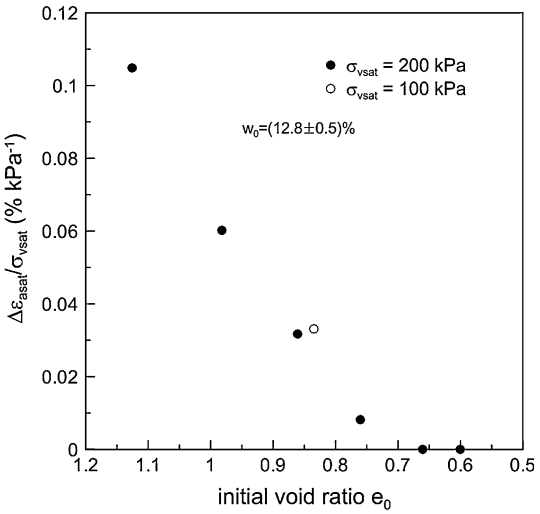

Fig. 2 Deformation on saturation at constant vertical stress for different initial void ratios (after Casini [4])

coalescence of aggregates into larger units. The information in Fig. 2 is, thus, extremely useful to define the limiting void ratio (around 0.6), above which the inter-grain porosity plays an important role.

3 Experimental programme

Twenty MIP tests were performed at five different void ratios e ($0.5 \leq e \leq 0.9$) above the limit previously indicated and at four gravimetric water contents w ($13\% \leq W \leq 21\%$). The detailed MIP programme is reported in Table 2, in which the water ratios e_w (volume of water over solid volume) and degrees of saturation of the different initial states are also included. The different initial states are plotted with solid symbols in the Proctor plane shown in Fig. 3a, together with the constant degree of saturation lines. Some MIP tests have been repeated by adding sodium chloride (NaCl) to the moulding water content in a concentration of 0.5 and 3 M (indicated by circles in Fig. 3, and with bold-underlined letters in Table 2). The addition of salt is expected to induce contraction of the microstructure, because the osmotic effects should be predominant in the microstructural domain and thus shifting of the dominant micropore size to lower dimensions (e.g. [17]). The ability to discern micro- and macroporosity is thus enhanced. Figure 3b shows the different compaction vertical stresses applied to achieve the different initial states. Static compaction stresses decrease with void ratio decrease and with the increase in the moulding water content.

MIP tests were performed on Pascal 140 and Pascal 440 apparatus from CE Instruments (France). Specimens were placed in a volume-calibrated glass vessel (dilatometer) and evacuated to about 0.03 kPa in the macropore unit (Pascal 140). Mercury was then added, and the pressure was increased continuously from vacuum to about 375 kPa. The dilatometer vessel was then transferred to the micropore unit of the porosimeter (Pascal 440). The pressure was increased stepwise to 400 MPa using pressure transmission oil. The intruded volumes were corrected for compressibility of mercury [35].

Environmental scanning electron microscopy (ESEM) was also used to qualitatively describe the arrangement of aggregation and particles, as well as the pore network properties, of the compacted samples. The ESEM investigation was performed using a FEI Quanta 600 ESEM at an average water vapour pressure in the specimen chamber of 70 and 372 Pa, room temperature of 25° corresponding to a relative humidity RH of 2.2 and 12%, respectively.

An oedometer test was performed to determine the water retention properties following the stress paths shown in Fig. 4. The stress paths allowed studying wetting and drying paths at two different initial void ratios ($e_0 = 0.82$

Table 2 Initial conditions in terms of void ratio e, gravimetric water content w (%), water ratio e_w and degree of saturation S_r

Water content w (%)	Void ratio e_0				
	0.50	0.60	0.67	0.80	0.90
13	$e_w = 0.350$	$e_w = 0.350$	$e_w = 0.350$	**$e_w = 0.350$**	$e_w = 0.350$
	$S_{r0} = 0.700$	$S_{r0} = 0.4153$	$S_{r0} = 0.583$	**$S_{r0} = 0.437$**	$S_{r0} = 0.389$
15	$e_w = 0.404$	$e_w = 0.404$	**$e_w = 0.404$**	$e_w = 0.404$	$e_w = 0.404$
	$S_{r0} = 0.808$	$S_{r0} = 0.583$	**$S_{r0} = 0.603$**	$S_{r0} = 0.505$	$S_{r0} = 0.449$
18	$e_w = 0.484$	**$e_w = 0.484$**	$e_w = 0.484$	$e_w = 0.484$	$e_w = 0.484$
	$S_{r0} = 0.968$	**$S_{r0} = 0.807$**	$S_{r0} = 0.722$	$S_{r0} = 0.605$	$S_{r0} = 0.538$
21	$e_w = 0.5$	$e_w = 0.565$	**$e_w = 0.565$**	$e_w = 0.565$	$e_w = 0.565$
	$w = 0.19$	$S_{r0} = 0.6921$	**$S_{r0} = 0.6575$**	$S_{r0} = 0.6262$	$S_{r0} = 0.5977$
	$S_{r0} = 1$				

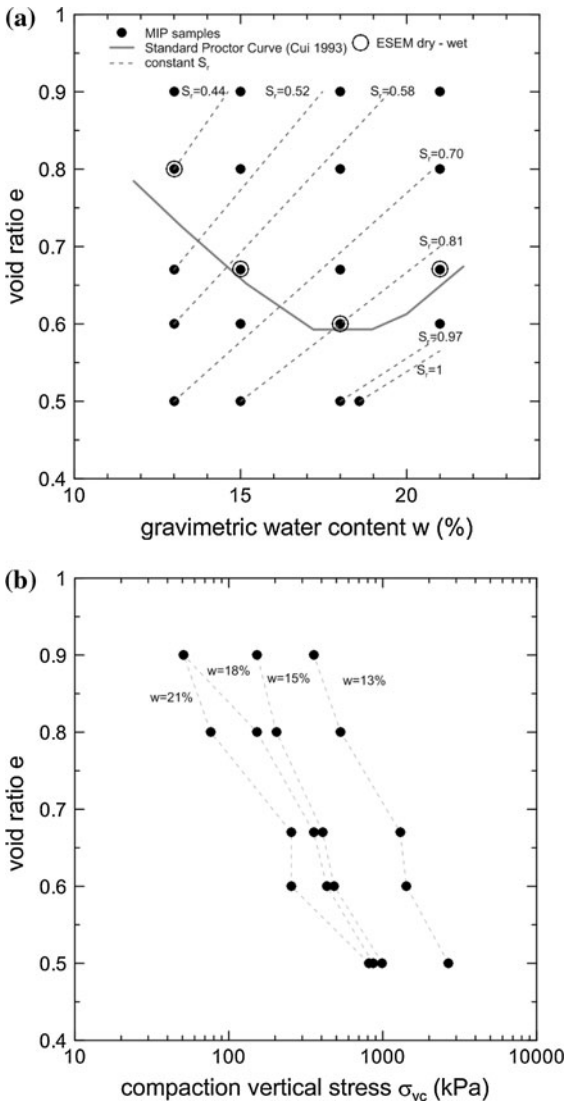

Fig. 3 Tested samples: **a** MIP samples (*full point*); MIP samples with salt (*circle*); ESEM with and without salt (*circle*); Proctor curve and iso-degree of saturation Sr in the plane w-e; **b** compaction vertical stress versus void ratio measured for compacted samples at target void ratio e and w

and 0.74, void ratio labelled during wetting and drying). The upper total suction range was also investigated by dew-point mirror psychrometer measurements (WP4, Decagon Device) carried out on compacted samples with initial void ratios ranging between 0.50 and 0.67 that underwent drying paths. The overall water retention data is plotted in Fig. 4, where void ratio effects are predominant in the low suction range [26].

4 MIP and ESEM results

The results of the MIP tests are usually reported in terms of cumulative and pore size density function versus entrance pore size (e.g. [13]). The cumulative mercury intrusion plot and different normalisation results of the PSD are reported in Fig. 5. The PSD in terms of log diameter has been normalised to the maximum intruded void ratio e_{nw} with

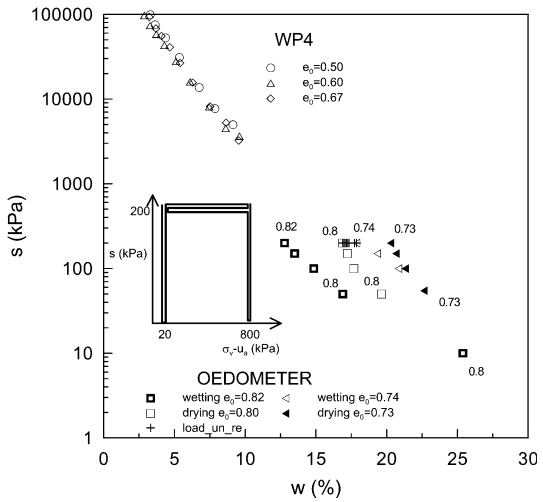

Fig. 4 Water retention properties of Jossigny silt under suction-controlled conditions complemented with psychrometer (WP4) measurements

non-wetting fluid to obtain a unit area below the curve (Fig. 5c). To compare the effect of the initial void ratio of the compacted material, the normalised density function was further scaled by this initial void ratio, as shown in Fig. 5d. This last plot PSD* was the one used to compare the effect of the initial state on the pore size distribution.

In Fig. 6, the PSD* results are presented for the different water contents and void ratios indicated in Fig. 3a. They were classified into groups with the same water content; and in each group, different void ratios were studied. It is interesting to note that for the lower water content of $w = 13\%$, the PSD* is mono-modal, and the peak value is centred on a diameter between 3 and 10 μm. This is rather unusual for clayey soil, and this unusual trend can be explained (supported by ESEM results Fig. 10a) because at this low water content, the aggregates are not fully developed, and the intra-aggregate porosity is hidden by the dominant inter-grain pores (associated with the pores between grains of the shielding skeleton). This dominant peak approximately coincides with the inter-grain pore size estimated from the particle size distribution (Fig. 1b).

As the water content increases, the dominant pore mode of the intra-aggregate domain emerges, and clear double-porosity networks are detected in Fig. 6b, c. On loading at $w_o = 15\%$, the macroporosity is consistently reduced, and the dominant macropore sizes shifted towards lower pore sizes. At $w_o = 18$ and 21%, the dominant and arising microporosity is shifted towards larger pore sizes. On loading at this higher water contents, not only the macroporosity is affected but also part of the micropore volume (refer to Fig. 6c, d).

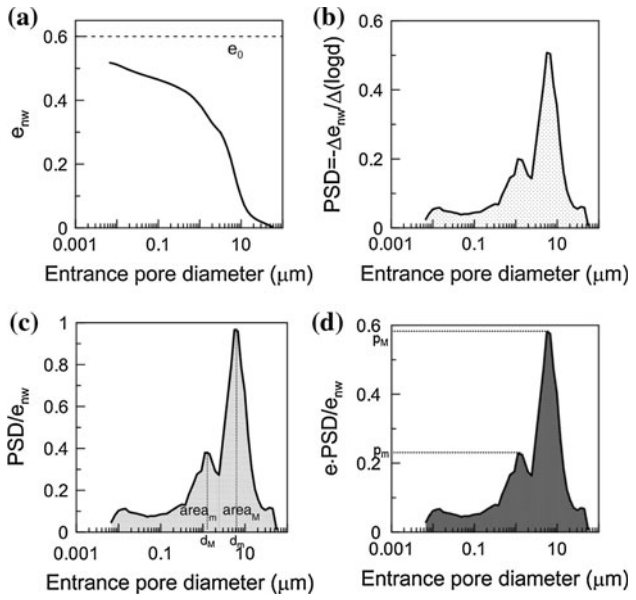

Fig. 5 **a** Intruded void ratio; **b** pore size density function (PSD); **c** PSD normalised with respect to the intruded void ratio (e_{nw}); **d** PSD normalised over e_{nw} and scaled to the void ratio e

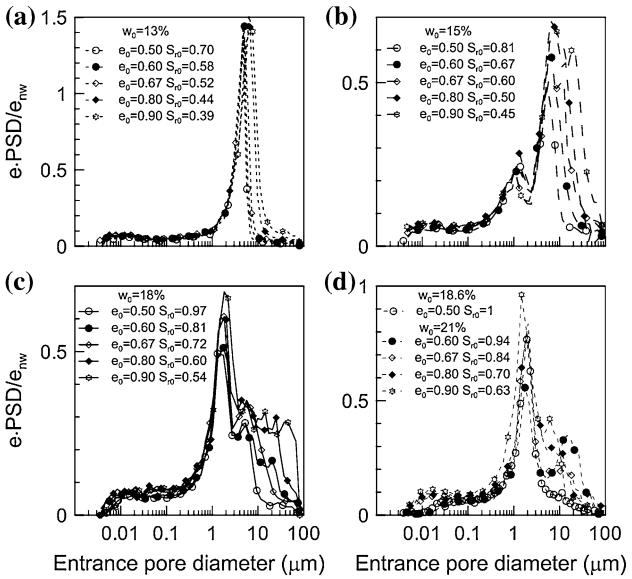

Fig. 6 Normalised PSD* curves for the same gravimetric water content: **a** $w = 13\%$; **b** $w = 15\%$; **c** $w = 18\%$; **d** $w = 21\%$

Similar results are also shown in Fig. 7, but grouped together in terms of void ratio. On wetting at constant void ratio, the microporosity emerges and progressively occludes the macroporosity. During this wetting, the initial monomodal structure observed at low water content progressively evolves towards a double-porosity network. These behavioural features are consistently observed at the different constant void ratios shown in Fig. 7.

Figure 8 shows the effects on the pore size distribution when saline water is added to the soil at different initial water contents and void ratios. The addition of salt induces the contraction of the aggregates (microporosity) and the shifting of the micropore size towards lower values, and thus enhancing the double-porosity network. For a given void ratio, the contraction of the microporosity induces the development of macroporosity, as shown in Fig. 8c, d for the higher water contents.

MIP results were interpreted using descriptors of the PSD* and their evolution as a function of the initial conditions (water content and void ratio). The descriptors used to characterise the evolution of the PSD* are indicated in Fig. 5, which correspond to:

- Peaks of the PSD* in terms of micro- and macroporosities (p_m and p_M Fig. 5d).
- Dominant pore modes of micro- and macroporosities (d_m and d_M Fig. 5c).
- Normalised pore volume corresponding to micro- and macroporosities (indicated as $area_m$ and $area_M$ in Fig. 5c, and corresponding to $area_m + area_M = 1$).

The evolution of the descriptors as a function of the initial state is indicated in Fig. 9. The peak values of the

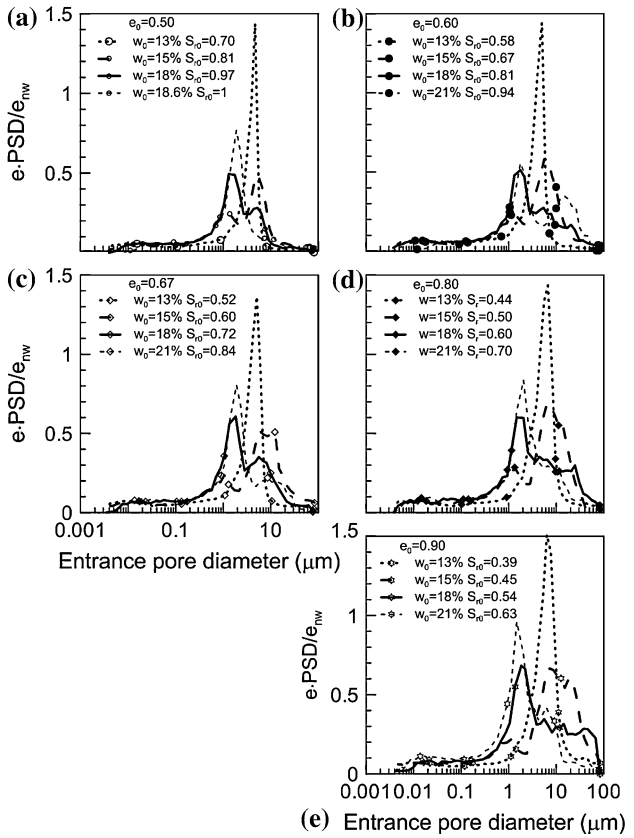

Fig. 7 Normalised PSD* curves for the same void ratio: **a** $e = 0.50$; **b** $e = 0.60$; **c** $e = 0.67$; **d** $e = 0.80$; **e** $e = 0.90$

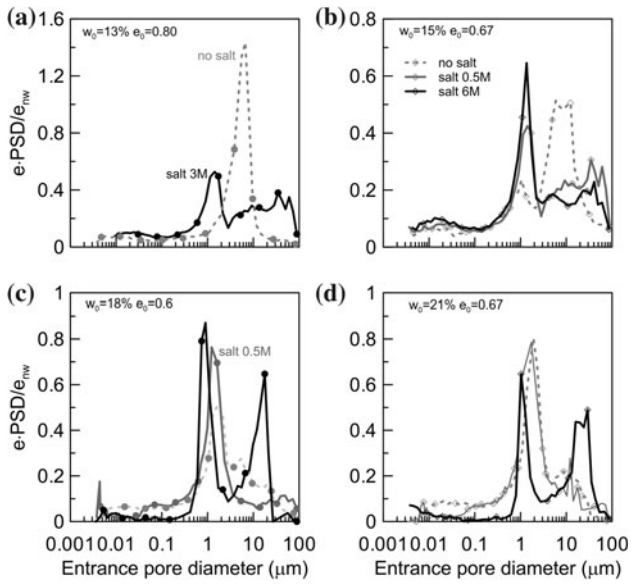

Fig. 8 Comparison of PSD curves for samples with and without the addition of salt (NaCl): **a** $w = 13\%$; $e = 0.80$; **b** $w = 15\%$; $e = 0.67$; **c** $w = 18\%$; $e = 0.6$; **d** $w = 21\%$; $e = 0.6$

macroporosity range of the PSD* decrease with increasing initial water content. An opposite trend is observed in the dominant peaks of the microporosity range, as a consequence of the expanding microstructure with water content. Equivalent trends are observed for the normalised micro- and macropore volumes in terms of their evolution with water content. On regarding the dominant pore mode of the microstructure, a slight shifting towards higher values is observed at larger initial water contents, which is also consistent with the expansion of the microporosity with water content. Some shifting of the dominant pore mode of the macroporosity towards larger values is also observed at higher water contents. This trend may be associated with some loss of the homogeneity of the sample during compaction at high water contents (sticky aggregates induced at high water contents). On regarding initial void ratio effects, both micro- and macroporosity peaks are decreased by compression. The dimensions of the dominant micropore sizes are also shifted towards lower dimensions on compression.

The arrangement of aggregations/particles and voids has been also investigated at their initial water content using environmental scanning electron microscopy (ESEM), which works under controlled environmental conditions [24]. Figure 10a, b presents the photomicrographs performed at two contrasting water contents ($w_0 = 13$ and 21%, respectively) and at the same void ratio ($e_0 = 0.80$). A double-porosity network is detected in the driest condition with well-defined inter-aggregate pores (around 10–20 μm), aggregations and particles. At higher water content, the aggregates increase their size and reduce the macropore volume, as shown in Fig. 10b.

The shielding skeleton formed by silt particles and aggregates connecting particles and filling inter-grain pores is clearly identified in Fig. 11a, b, in which the driest state ($w_0 = 13\%$) is presented at two void ratios ($e_0 = 0.8$ and 0.9, respectively). On compression, the macroporosity appears to be reduced when comparing both photomicrographs.

The microstructural investigation was extended to samples that were prepared with saline water. As observed in Fig. 12 at $w_0 = 15\%$, a denser microstructure is induced due to the contraction of the aggregates, in which clear inter-aggregate pores are detected (the addition of salt induces the enhancement of the double-porosity features).

5 Water retention properties based on MIP results

The MIP results can be used to obtain the relationship between the suction and the degree of saturation or water content at constant void ratio. The mercury intrusion is assimilated to the air intrusion (non-wetting fluid) during the drying path of the water retention curve. Thus, the injection of mercury with a contact angle is equivalent to the drainage of the water induced by air front advancing for

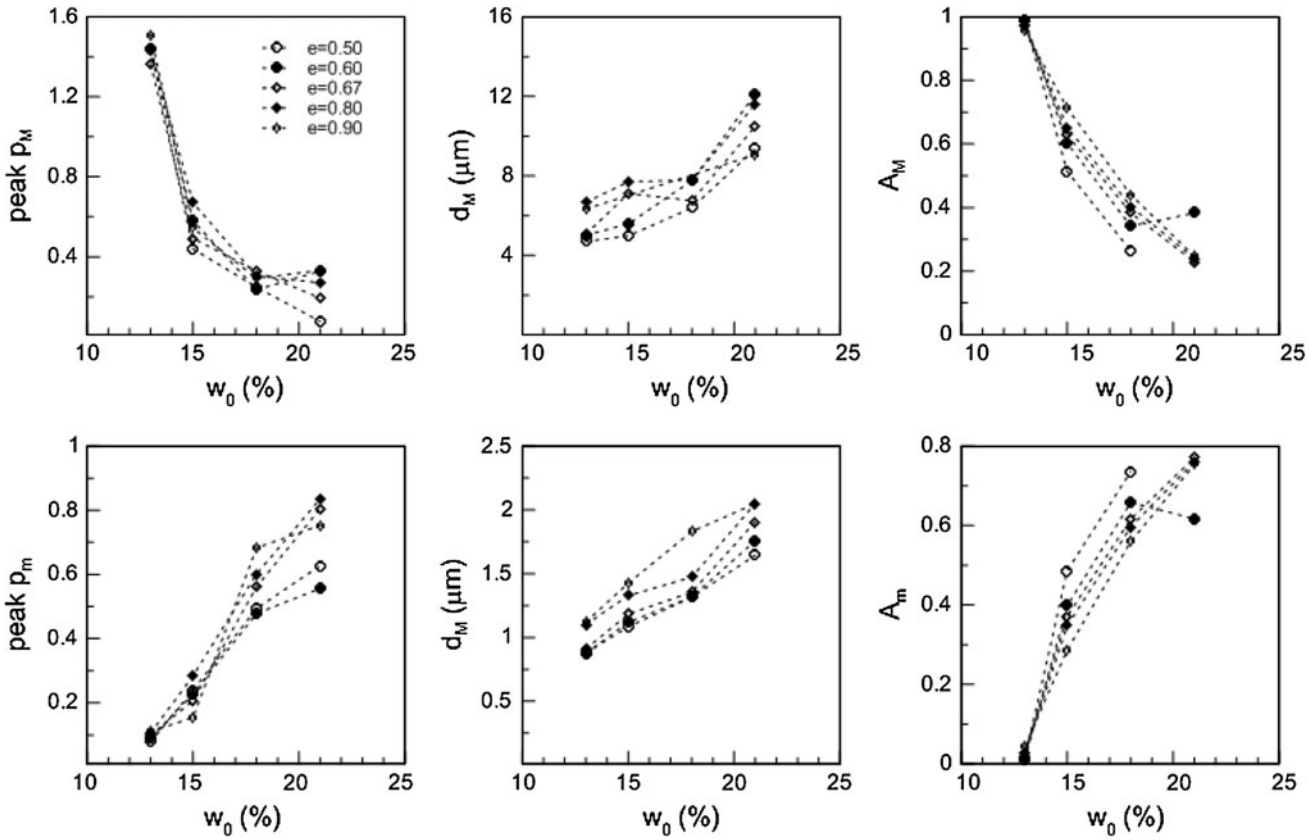

Fig. 9 PSD* parameters versus gravimetric water content

the same diameter of pores intruded. Under the hypothesis of non-deformable soil skeleton, the volume of pores non-intruded by the mercury should be used to evaluate the degree of saturation or the water content corresponding to the equivalent applied air overpressure. Anyway, the non-intruded porosity by the mercury should be taken into account for estimating the residual water content in the evaluation of the water content [24]. The WRC obtained is valid in the range where the capillarity is the predominant physical mechanism, usually for suction $s < 2$ MPa [24].

The water ratio $e_w = V_w/V_s = S_r \cdot e$ is estimated by the following equations:

$$e_{nw} + e_w = e; \quad e_w = e - e_{nw} = (1 - S_{rnw}) \cdot e \tag{1}$$

where e_{nw} is the non-wetting ratio (mercury) and S_r and S_{rnw} the degree of saturation of water and non-wetting fluid, respectively ($S_r + S_{rnw} = 1$ for a two fluid mixture). In Fig. 13, the WRCs obtained after the correction that takes into account the non-intruded porosity and the adsorbed water are reported. The residual water ratio has been taken $e_{wres} = 0.25$ in agreement with measurements performed with a WP4 at different void ratios.

The results are reported in the plane water ratio e_w—suction s for the same water content (Fig. 13a) and the same void ratio (Fig. 13b). As the void ratio decreases, the air entry value increases, and the curves are steeper. This trend is consistent for the four gravimetric water contents investigated (Fig. 13a). The increase in the compaction water content let the curves more dispersed in the higher range of suctions ($s \geq 100$ kPa).

The driest samples ($w = 13\%$) show a more rigid behaviour before the air entry value, after that the curves show a less steep trend compared to the wettest samples (Fig. 13b). This behaviour persisting for the five void ratios is explored. For the same compaction water content, the form of the curves is similar, while the void ratio affects the air entry values of the curves.

Usually the WRC obtained for the different types of soil is best fitted with original or modified van Genuchten [33] or Brooks and Corey [3] models without taking into account the heterogeneity of the pore systems (e.g. [2, 25, 28, 32]). Here the heterogeneity of the pore system induced by the compaction process is taken into account using a multimodal retention model, defined by Durner [9] as a linear superposition of subcurves of the van Genuchten type with the following equation:

$$E_w = \frac{e_w - e_{wres}}{e - e_{wres}} = \sum_{i=1}^{k} w_i \left[\frac{1}{1 + (\alpha_i \cdot s)^{n_i}} \right]^{m_i} \tag{2}$$

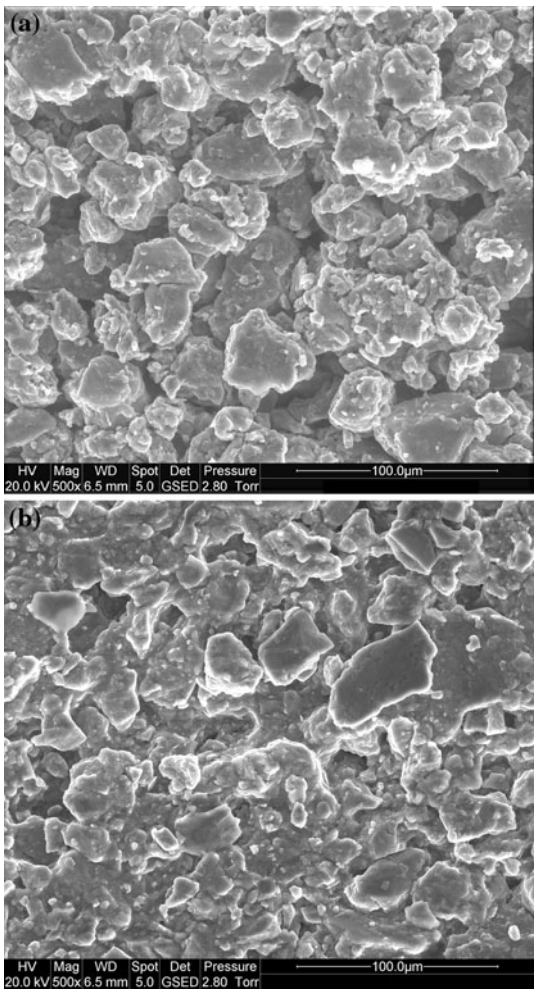

Fig. 10 ESEM on Jossigny silt with void ratio $e = 0.80$: **a** water content $w = 13\%$; **b** water content $w = 21\%$

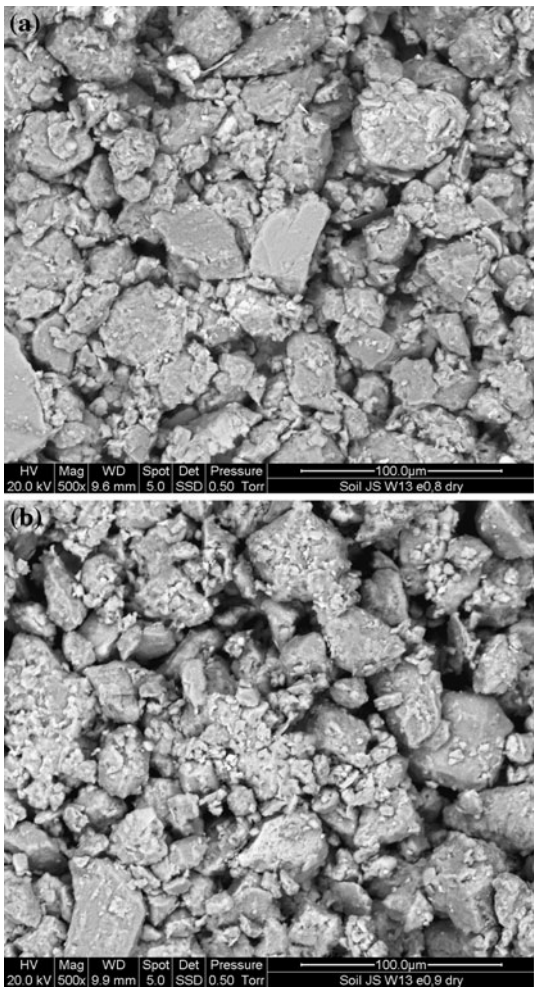

Fig. 11 Shielding effect at water content $w = 13\%$: **a** void ratio $e = 0.80$; **b** void ratio $e = 0.90$

where k is the number of subsystems that assembled together give the global pore size distribution, w_i are weighting factors for each subcurve subject to $0 < w_i < 1$ and $\sum w_i = 1$. For the parameters of the subcurves (α_i, n_i, m_i) must be imposed the condition $\alpha_i > 0$, $m_i > 0$, $n_i > 1$. Here, the additional constraint $n_i = 1/(1 - m_i)$ is imposed.

Each subcurve in Eq. 2 differentiated two times with respect to the suction s gives the relationship between the suction at the inflection point and the parameters given by the following expression:

$$s_{pi} = \frac{m_i^{1-m_i}}{\alpha_i} \tag{3}$$

where s_{pi} is the suction at the inflection point in the E_w-s plane. Once α_i is obtained, from Eq. 3 and substituting in Eq. 2, the water storage mechanism in a heterogeneous porous medium becomes:

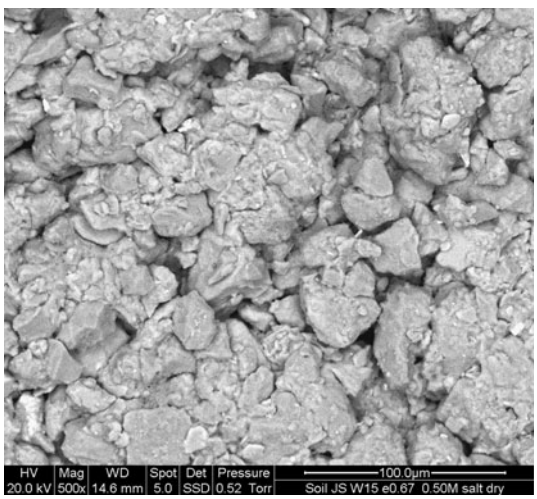

Fig. 12 Effect of the addition of NaCl on the microstructure of Jossigny silt

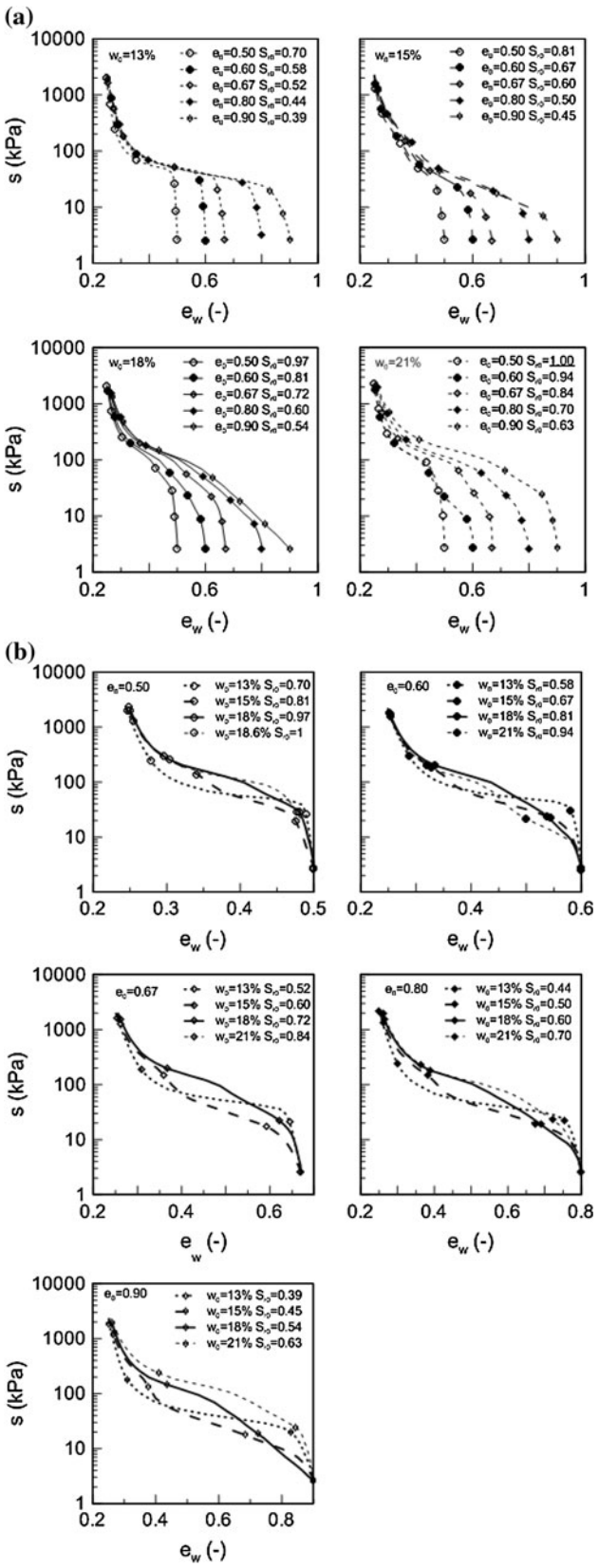

Fig. 13 Drying paths deduced from MIP: **a** for the same water content; **b** for the same void ratio

$$E_w = \frac{e_w - e_{wres}}{e - e_{wres}} = \sum_{i=1}^{k} w_i \left[1 + m_i \cdot \left(\frac{s}{s_{pi}} \right)^{1/(1-m_i)} \right]^{-m_i} \quad (4)$$

Equation 4 is used to model the WRC data obtained by MIP. The experimental data are modelled with a bimodal water retention model, obtained setting $k = 2$ in the above equation.

The pore capillary density function (PCF) is defined as:

$$\mathrm{PCF} = \Delta E_w / \Delta \log(s) \quad (5)$$

where E_w is the effective degree of saturation as defined in Eq. 4.

The model is calibrated by best fitting the PCF obtained in experimental results as shown in Fig. 14a. The area below the peak of lower suction is defined as w_1 (macro area below the PCF), while w_2 (micro area) is given by $w_2 = 1 - w_1$ because the area below the curve corresponds to the unity. The suction at inflection points are named, respectively, s_{pM} and s_{pm} as reported in Fig. 14a. The experimental data and the model prediction are compared in Fig. 14b, and the model fits well the experimental results in the entire range of suction. Furthermore, the model is able to capture well the change in shape of the retention curve at the inflection points. The experimental results in Fig. 15 is well fitted by Eq. 4.

The macro area shows an interesting trend, which decreases as the water content increases (Fig. 16) and increases with void ratio.

6 Interpretation of water retention properties: MIP versus oedometer results

The parameters obtained by the multimodal model have been calibrated as a function of void ratio and gravimetric water content. The macro area w_1 has been related to the water content w through the following equation:

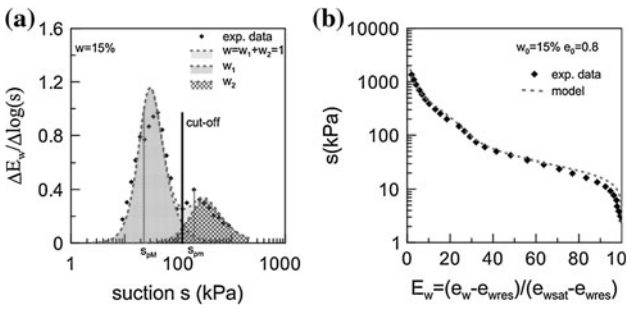

Fig. 14 Laboratory versus model results: **a** Macro- and micropore capillary functions (PCF); **b** water retention curve derived from PCF

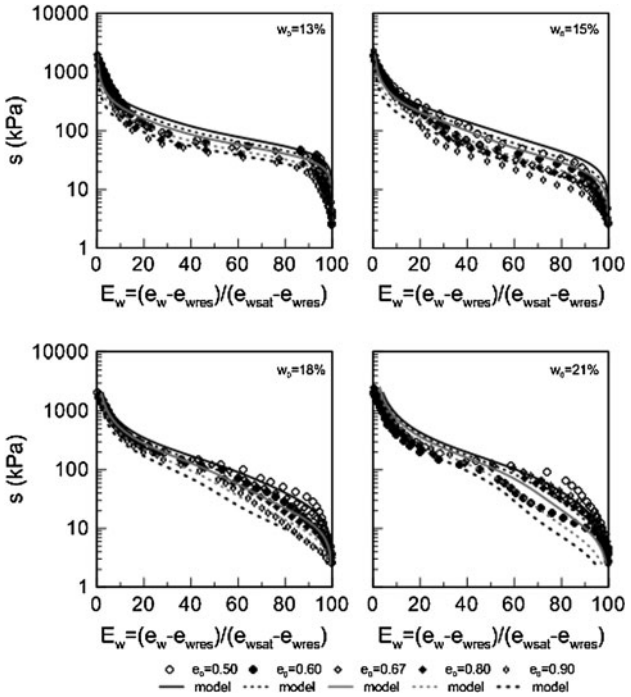

Fig. 15 Comparison between model and experimental data for different gravimetric water contents

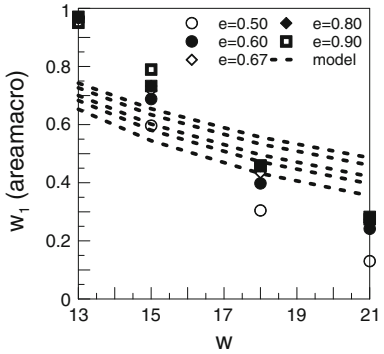

Fig. 16 Comparison between model and experimental results: area macro versus gravimetric water content

$$w_1(\text{area macro}) = (w_{\text{res}}/w)^{\alpha} \tag{6}$$

where $\alpha = (\text{par}_1 \cdot e)^{\text{par}_2}$ and $w_{\text{res}} = e_{\text{wres}}/G_s = 0.25/2.69 = 0.0929$, which is the residual water content of the soil. The values of the different parameters are reported in Table 3. The comparison between MIP data and the model (in dotted line) is presented in Fig. 17.

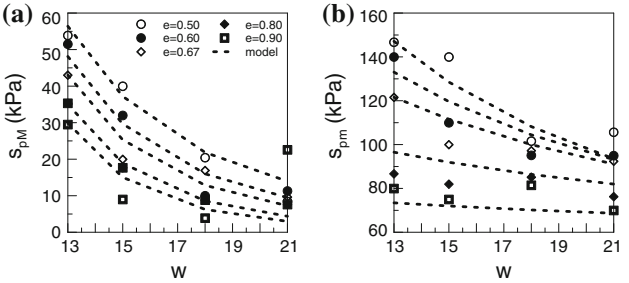

Fig. 17 Comparison between MIP data and model results of peak value of suction as a function of water content: **a** Macro; **b** micro

Also the suction at inflection points for micro and macro domains have been related to the water content and void ratio through similar equations:

$$s_{\text{pM}} = A \cdot (w_{\text{res}}/w)^{\beta}, \quad s_{\text{pm}} = B \cdot (w_{\text{res}}/w)^{\delta} \tag{7}$$

where $A = \text{par}_3$, $\beta = \text{par}_4 \cdot e + \text{par}_5$, $B = \text{par}_6 \cdot e + \text{par}_7$ and $\delta = \text{par}_8 \cdot e + \text{par}_9$.

The gradient of the macro m_{M} and micro m_{m} retention functions has been related to the void ratio and water content with the equations:

$$m_{\text{M}} = (w_{\text{res}}/w)^{\text{par}_{10}} \quad \text{and} \quad m_{\text{m}} = \text{par}_{11} \cdot (w_{\text{res}}/w)^{\text{par}_{12}} \tag{8}$$

The values of the different parameters are given in Table 3.

The data of drying path obtained under suction-controlled conditions and oedometer conditions have been compared with the model prediction in Fig. 18. Two drying curves have been simulated, one for the path at lower density (void ratio at the beginning of the drying path $e_0 = 0.80$) and the second for the path at higher density (void ratio $e_0 = 0.73$). Curves have been normalised in order to fit the initial and final water contents of each path.

The evolution is reasonably reproduced by the model for both changes in suction and vertical load.

7 Conclusions

An extended microstructural investigation (mercury intrusion porosimetry MIP and electron micrographs) has been performed on statically compacted Jossigny silt at different initial void ratios and water contents. The objective was to obtain a deeper understanding of the evolution of the microstructural changes on a silty soil and their consequences

Table 3 Bimodal retention model parameters

par_1	par_2	par_3 (kPa)	par_4	par_5	par_6 (kPa)	par_7 (kPa)	par_8	par_9	par_{10}	par_{11}	par_{12}
1.36	0.61	150	4.73	0.54	-312	358	−2.01	1.95	0.99	0.75	0.45

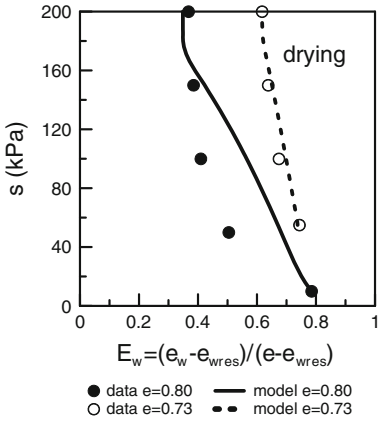

Fig. 18 Comparison along drying paths between experimental data under suction-controlled conditions and model predictions

on the water retention properties. As highlighted by the experimental results, the shape of the PSD is essentially controlled by the compaction water content. The PSDs are basically bimodal in the range of water contents and void ratios tested. At low water contents, the microporosity decreases and the PSD tends to a quasi-monomodal distribution for the driest compaction. At higher water contents, more and more aggregates are created by the compaction process, which induces the emergence of an increasingly pronounced peak around 2 μm in the PSD. For wet samples, aggregates form a shielding skeleton around the sand/silt particles (confirmed by ESEM micrographs), and the PSD recovers a monomodal distribution. When compacted with saline solution, the material presents a more pronounced double-porosity, as a result of aggregate shrinkage.

The drying path of the water retention curve obtained by MIP has been modelled with a multimodal retention model, where the weighted parameters are related to the area below the pore capillary distribution and the suctions at inflection points to the peak value of the distribution. The agreement between the measured and the estimated WRC indicates that the multimodal prediction method leads to more realistic estimation of the retention properties of soils. The model parameters are related to the pore capillary distribution and have a clear physical meaning. The model has been satisfactorily used to reproduce the suction-water content path during drying at different initial void ratios and under oedometer conditions.

The research work highlights the importance of modelling the double-porosity development during compaction, even for non-plastic materials, and proposes a flexible model to capture the retention curve resulting from microstructural features.

Acknowledgments The authors acknowledge Michael Plötze and Gabriele Peschke of Institute of Geotechnical Engineering at ETHZ for their technical support in performing the MIP and ESEM tests, respectively.

References

1. Aubertin M, Mbonimpa M, Bussière B, Chapuis RP (2003) A model to predict the water retention curve from basic geotechnical properties. Can Geotech J 40:1104–1122
2. Barbour SL (1998) The soil-water characteristic curve: a historical perspective. Can Geotech J 35:873–894
3. Brooks RH, Corey AT (1964) Hydraulic properties of porous media. Colo State Univ Hydrol Paper 3:1–27
4. Casini F (2008) Effetti del grado di saturazione sul comportamento meccanico di un limo. PhD thesis, Universitá degli Studi di Roma "La Sapienza", Italy
5. Cui YJ (1993) Etude du comportement d'un limon non saturé et de sa modélisation dans un cadre élasto-plastique. PhD thesis, Ecole Nationale des Ponts et Chassées, Paris, France
6. Cui YJ, Delage P (1996) Yielding and plastic behavior of an unsaturated compacted silt. Géotechnique 46(2):291–311
7. Delage P (2010) A microstructure approach to the sensitivity and compressibility of some Eastern Canada sensitive clays. Géotechnique 60(5):353–368
8. Delage P, Audiguier M, Cui YJ, Howat M (1996) The microstructure of a compacted silt. Can Geotech J 33:150–158
9. Durner W (1994) Hydraulic conductivity estimation for soils with heterogeneous pore structure. Water Resour Res 30(2):211–223
10. Gallipoli D, Wheeler S, Karstunen M (2003) Modelling the variation of degree of saturation in a deformable unsaturated soil. Géotechnique 53(1):105–112
11. Gens A, Alonso E, Suriol J, Lloret A (1995) Effect of structure on the volumetric behaviour of a compacted soil. In: Proceedings of 1st international conference on unsaturated soils, Paris
12. Juang CH, Holtz RD (1986) Fabric, pore size distribution, and permeability of sandy soils. J Geotech Eng Div ASCE 112(9): 855–868
13. Koliji A, Vuillet L, Laloui L (2010) Structural characterization of unsaturated aggregated soil. Can Geotech J 47:297–311
14. Lapierre C, Leroueil S, Locat J (1990) Mercury intrusion and permeability of Louisville clay. Can Geotech J 27:761–773
15. Leroueil S, Bouchlin G, Tavenas F, Bergeron L, La Rochelle P (1990) Permeability anisotropy of natural clays as a function of strain. Can Geotech J 27:568–579
16. Mašín D (2010) Predicting the dependency of a degree of saturation on void ratio and suction using effective stress principle for unsaturated soils. Int J Numer Anal Meth Geomech 34:73–90
17. Mayne C, Murad M (2003) Macroscopic behavior of swelling porous media derived from micromechanical analysis. Transp Porous Media 50:127–151
18. Mbonimpa M, Aubertin M, Bussière B (2006) Predicting the unsaturated hydraulic conductivity of granular soils from basic geotechnical properties using the modified Kovács (MK) model and statistical models. Can Geotech J 43:773–787
19. Miller GA, Khoury CN, Muraleetharan KK, Lui C, Kibbey TCG (2008) Effects of soil skeleton deformations on hysteretic soil water characteristics curves: experiments and simulations. Water Resour Res 44:1–10. doi:10.1029/2007WR006492
20. Monroy R, Zdravkovic L, Ridley A (2010) Evolution of microstructure in compacted London clay during wetting and loading. Géotechnique 60(2):105–119
21. Nuth M, Laloui L (2008) Advances in modelling hysteretic water retention curve in deformable soils. Comput Geotech 35:835–844
22. Or D (1996) Wetting-induced soil structural changes: the theory of liquid phase sintering. Water Resour Res 32(10):3041–3049

23. Richard G, Cousin I, Sillon JF, Bruand A, Guérif J (2001) Effect of compaction on the porosity of a silty soil: influence on unsaturated hydraulic properties. Eur J Soil Sci 52:49–58
24. Romero E, Simms PH (2008) Microstructure investigation in unsaturated soils: a review with special attention to contribution of mercury intrusion porosimetry and environmental scanning electron microscopy. Geotech Geol Eng 26(6):705–727
25. Romero E, Vaunat J (2000) Retention curves of deformable clays. In: Proceedings of international workshop on unsaturated soils: experimental evidence and theoretical approaches, Balkema, Trento, pp 91–106
26. Romero E, Lloret A, Gens A (1999) Water permeability, water retention and microstructure of unsaturated Boom clay. Eng Geol 54:117–127
27. Romero E, Della Vecchia G, Jommi C (2011) An insight into the water retention properties of compacted clayey soils. Géotechnique 61(4):313–328
28. Salager S, El Youssoufi MS, Saix C (2010) Definition and experimental determination of a soil water retention surface. Can Geotech J 47(6):609–622
29. Simms PH, Yanful EK (2004) Estimation of soil-water characteristic curve of clayey till using measured pore-size distributions. J Geotech Eng Div ASCE 130(8):847–854
30. Simms PH, Yanful EK (2005) A pore-network model for hydromechanical coupling in unsaturated compacted clayey soils. Can Geotech J 42:499–514
31. Tarantino A (2009) A water retention model for deformable soils. Géotechnique 59(9):751–762
32. Tarantino A (2010) Compacted versus reconstituted states. In: Proceedings of 5th international conference on unsaturated soils, Balkema, Barcelona, pp 113–136
33. van Genuchten MT (1980) A closed-form equation for predicting the hydraulic conductivity of unsaturated soil. Soil Sci Soc Am J 44:892–898
34. Vicol T (1990) Comportment hydraulique et mecanique d'un sol fin non sature application a la modelisation. PhD Thesis, Ecole Nationale des Ponts et Chassées, Paris, France
35. Weber TM, Plötze M, Laue J, Peschke G, Springman (2010) Smear zone identification and soil properties around stone columns constructed in-flight in centrifuge model tests. Géotechnique 60(3):197–206